Author Manuscript

Conductive Passivator and Dipole Layer Mixture Enabling High-Performance Stable Perovskite Photoelectrode-Based Solar Water Splitting

*Juwon Yun, Hyungsoo Lee, Young Sun Park, Wooyong Jeong, Chang-Seop Jeong, Junwoo Lee, Jeongyoub Lee, Jeiwan Tan, Sunhil Ma, Gyumin Jang, Chan Uk Lee, Subin Moon, Hayoung Im, Soobin Lee, Dong-Yub Yee, Ji-Hee Kim, and Jooho Moon**

J. Yun, Dr. H. Lee, Y. S. Park, J. Lee, J. Lee, G. Jang, Dr. J. Tan, C. U. Lee, S. Moon, H. Im, S. Lee, C-S. Jeong, Prof. J. Moon

This is the author manuscript accepted for publication and has undergone full peer review but has not been through the copyediting, typesetting, pagination and proofreading process, which may lead to differences between this version and the Version of Record. Please cite this article as doi: 10.1002/aenm.202301693.

This article is protected by copyright. All rights reserved.

Department of Materials Science and Engineering, Yonsei University

50 Yonsei-ro Seodaemun-gu, Seoul, 03722, Republic of Korea

E-mail: jmoon@yonsei.ac.kr

Dr. S. Ma

Department of Chemical Engineering

University of Michigan

Ann Arbor, MI, 48109, USA

D-Y. Yee

Department of Energy Science, Sungkyunkwan University

Suwon 16419, Republic of Korea

Prof. J-H. Kim

Department of Physics, Pusan National University

Author Manuscript

This article is protected by copyright. All rights reserved.

Busan 46241, Republic of Korea

*Corresponding author

E-mail: jmoon@yonsei.ac.kr

Keywords: perovskite photoanode, interface engineering, conductive passivation, interface dipole, unbiased water splitting

Abstract

Recently, lead halide perovskites have attracted significant attention as promising absorber materials for photoelectrochemical (PEC) solar water splitting. However, charge-accumulation-induced ion migration at the interface causes perovskite degradation and efficiency loss. To suppress the charge accumulation and improve the PEC performance of the perovskite photoanode, we propose a simple interface engineering by decorating the SnO_2/perovskite interface with a mixture of polyethylenimine ethoxylated (PEIE) and chlorobenzenesulfonic acid (CBSA). The mixed CBSA+PEIE treatment effectively passivates

This article is protected by copyright. All rights reserved.

Author Manuscript

the oxygen vacancies in SnO_2 and adjusts the band alignment between SnO_2 and the perovskite. The synergistic effects of the mixture treatment facilitate an effective carrier extraction at the SnO_2/perovskite interface, enhance the PEC performance, and improve the stability of the device. The perovskite photoanode exhibited an impressive applied bias photon-to-current efficiency of 12.9% with an outstanding durability for 225 h. Furthermore, an unbiased solar water splitting was achieved using all the perovskite photoelectrodes, resulting in a remarkable unassisted solar-to-hydrogen efficiency of 10.9 % and a continuous 22 h stable operation.

Author Manuscript

This article is protected by copyright. All rights reserved.

Author Manuscript

1. Introduction

In 2015, the Paris Climate Accords were adopted to regulate the rise in the mean global temperature to below 2 °C (3.6 °F) and eventually realize zero CO_2 emission. These goals can be achieved by developing sustainable and renewable clean energy. Photoelectrochemical (PEC) bias-free tandem devices, comprising a front photoanode stacked with a back photocathode, have emerged as promising candidates for realizing an efficient solar-to-hydrogen (STH) conversion.[1, 2] In the past few decades, photocathodes have undergone rapid advances in terms of photocurrent and onset potential enhancements. By contrast, the development of photoanodes has remained almost stagnant with insufficient improvements owing to the constituting materials' short hole-diffusion lengths, low carrier mobilities, and sluggish kinetics of oxygen evolution reaction (OER) compared to those of the hydrogen evolution reaction (HER).[3–5] Intensive efforts such as nanostructuring, heterojunction engineering, doping, and passivation strategies have been dedicated to improve the performance of n-type semiconductors including TiO_2, Fe_2O_3, Ta_3N_5, and WO_3.[6-9] Among the various known n-type photoanode candidates,

This article is protected by copyright. All rights reserved.

Author Manuscript

bismuth vanadate ($BiVO_4$), in a tandem configuration, is considered as a state-of-the-art absorber owing to its high photovoltage of over 1 V and stable property in neutral electrolytes.[10] However, the STH efficiency in a $BiVO_4$-based PEC tandem device still falls short of 5 % and is insufficient for practically using hydrogen energy through PEC water splitting.[11]

Lead halide perovskite is considered a next-generation absorber for photovoltaics (PVs) to achieve >25 % power-conversion efficiencies (PCEs).[12] Compared with the conventional n-type semiconductors, lead halide perovskite exhibits an excellent hole mobility and a long hole-diffusion length.[13] In addition, triple cation based lead halide perovskite has a suitable bandgap (~1.6 eV) along with high performance parameters such as ~ 1 V photovoltage and ~ 20 mA cm^{-2} photocurrent density, which makes it promising absorber as compared with $BiVO_4$. To prevent moisture-induced damages and improve the stability of perovskite-based photoelectrodes, various protective strategies such as metal encapsulation, liquid metal coating, conductive epoxy coating, and carbon paste incorporation have been introduced.[14–22] For example, thin Ni and field metals utilized as

This article is protected by copyright. All rights reserved.

Author Manuscript

physical protectors to prevent moisture intrusion into perovskite photoanodes impart an operational durability of less than 10 h.[19, 20] Cameron and coworkers demonstrated long-term operational stability of a perovskite photoanode for 30 h using a thick mesoporous carbon and graphite nanosheet to prevent water degradation.[21] Nevertheless, a significant photovoltage loss was observed, which resulted in a poor onset potential. Kim *et. al* conducted metal encapsulation using Ni foils with carbon powder to inhibit water permeation and achieved an operational stability of 48 h (J/J_i ~60 %, J_i: initial photocurrent density) as well as a high applied bias photon-to-current efficiency (ABPE).[22] Although several successful protection strategies have been developed to date, the stability and onset potential of perovskite photoanodes are still inferior to those of $BiVO_4$. In addition, the degradation mechanism of perovskites during a PEC operation remains under-explored.

Ion migration is reportedly the primary cause of efficiency loss and degradation in perovskite solar cells and light-emitting diodes.[23, 24] This phenomenon can induce phase segregation, which eventually leads to the formation of undesirable compounds, and this

This article is protected by copyright. All rights reserved.

Author Manuscript

formation rate is particularly accelerated at the interface, where the defect-induced charges accumulate.[25–28] We believe that ion migration is responsible for the instability and onset potential loss in perovskite photoanodes. A perovskite photoanode is composed of an n-i-p structure, and this, the surface chemistry and electrical property of the electron transport layer (ETL) can critically influence the defect states of the perovskite. Further, perovskites are characterized by a large effective mass around the conduction band, because of which the accumulation of electrons is more favored at the ETL/perovskite interface, and hence, the electron mobility of perovskites is lower than their hole mobility.[29, 30] An effectively engineered ETL/perovskite interface can facilitate electron extraction and improve the photoelectrode performance. According to previous studies, conjugated organic compounds with different functional groups such as sulfonic acid (-SO_3), amine (-NH_2), and halide (-F, -Cl, -Br, and -I) can effectively passivate the surface defects on the perovskite and ETL in perovskite solar cells.[31–34] Furthermore, the introduction of an interfacial dipole to tune the band alignment across the interface can also enhance the charge extraction.[35]

This article is protected by copyright. All rights reserved.

Author Manuscript

Herein, we propose a simple interface engineering approach based on the combination of a dipole layer and conductive passivation to adjust the band alignment as well as to passivate interfacial defects. A mixture of polyethylenimine ethoxylated (PEIE) and chlorobenzenesulfonic acid (CBSA) is introduced at the SnO_2/perovskite interface, wherein PEIE and CBSA acted as the dipole layer and conductive passivator, respectively. PEIE, a polyelectrolyte, is widely used to reduce the work functions of metal oxides in PVs because of its ability to provide interfacial dipoles.[36, 37] CBSA is highly conductive with two functional groups, viz. the sulfonic acid (-SO_3) and chloride (-Cl) groups, that effectively induce coordination among the oxygen and halide vacancies in SnO_2 and the perovskite, respectively.[38, 39] The addition of CBSA to the PEIE dipole layer effectively passivates the oxygen vacancies in SnO_2 as well as enhances the conductivity of PEIE while maintaining its interfacial dipole effect. The synergy between the PEIE dipole interlayer and the CBSA molecule facilitates carrier extraction at the SnO_2/perovskite interface, reduces hysteresis, and enhance the PEC performance and operational stability of the device. The resulting interface-engineered perovskite photoanode exhibited an onset potential of 0.34 V versus the reversible hydrogen electrode (RHE), a saturated photocurrent density of 22.7 mA cm-

This article is protected by copyright. All rights reserved.

^{2} at 0.7 V_{RHE}, and a superior ABPE value of 12.9% at 0.57 V_{RHE} in 1 M KOH (pH 14). Furthermore, our perovskite photoanode exhibited a remarkably extended lifetime of 225 h and successfully retained ~70% of the initial photocurrent at 1.23 V_{RHE} under continuous 1-sun illumination. By connecting with the inverted-type perovskite photocathode, we successfully demonstrated an unbiased photoelectrode device consisting of all-perovskite photoelectrodes connected in a parallel configuration. This fabricated device showed a remarkable unassisted STH efficiency of 10.9% with stable operation for 22 h and sustained ~70% of the initial photocurrent.

2. Results and Discussion

Figure 1a illustrates the device configuration of the perovskite solar cell (PSC) and perovskite photoanode fabricated in this study. The PSC has an indium tin oxide (ITO)/SnO_2/perovskite/spiro-OMeTAD/Au structure. Triple-cation perovskite ($FA_{0.80}MA_{0.15}Cs_{0.05}PbI_{2.55}Br_{0.45}$) (denoted as PSK) was selected to form the absorber layer owing to its high humid resistance and thermal stability.[40] To improve carrier extraction

This article is protected by copyright. All rights reserved.

Author Manuscript

Author Manuscript

at the SnO_2/PSK interface, we applied two different treatments, *i.e.*, treatment with PEIE molecules and that with a mixture of PEIE and CBSA molecules, on the SnO_2 layer (denoted as PEIE-SnO_2 and mixed-SnO_2, respectively). The reference sample (denoted as ref-SnO_2) was fabricated without any ETL interface treatment. To evaluate the interface treatment effect, the champion performances of the PSCs w/ref-SnO_2, w/PEIE-SnO_2, and w/mixed-SnO_2 were analyzed, and the corresponding results are shown in Figure 1b. The PSC w/ref-SnO_2 exhibits a maximum PCE of 17.71 %, an open circuit voltage (V_{OC}) of 1.06 V, a short-circuit current density (J_{SC}) of 21.89 mA cm^{-2}, and a fill factor (FF) of 76.53. By contrast, the PSC w/PEIE-SnO_2 exhibits a maximum PCE of 18.71%, which is higher than that of the PSC w/ref-SnO_2 sample, indicating that the performance of the PSC w/PEIE-SnO_2 is higher than that of the reference sample. Interestingly, the PCE of the PSC w/mixed-SnO_2 sample further increases to 20.31%, and the corresponding V_{OC} and J_{SC} values are significantly improved compared to those of the PSC w/PEIE-SnO_2 (Table S1, Supporting Information). The PSC performance was additionally evaluated by varying the PEIE concentration (*i.e.*, 0.01, 0.025, 0.05, and 0.1 wt%) and CBSA concentration (*i.e.*, 2, 5, 10, and 20 mM) to optimize the interface treatment concentration (Figure S1, Supporting Information). To

This article is protected by copyright. All rights reserved.

Author Manuscript

confirm reproducibility of the results, 15 samples were evaluated, and the statistics of their performance parameters were determined from their corresponding *J–V* curves under each condition (Figure S2, Supporting Information). The results show that the average PCE is enhanced in the order of PSC w/ref-SnO_2 < w/PEIE-SnO_2 < w/mixed-SnO_2, whereas the average FF values are nearly identical irrespective of the interface treatment conditions. Consequently, it can be concluded that the observed PCE improvement originates from the increase in both V_{OC} and J_{SC}. Next, the hysteresis behavior was evaluated to determine the amount of charge accumulated at the ETL/PSK interface (Figure S3, Supporting Information).[41] We performed the *J-V* measurements at various scan rates of slow (0.08 V/s), intermediate (0.5 V/s), and fast (2.5 V/s). As shown in Figure S3, hysteresis was observed for all scan rates, irrespective of the interfacial treatment (PEIE-SnO_2, mixed-SnO_2). However, the magnitude of hysteresis was significantly reduced when interface was treated. We also calculated hysteresis index (HI) as follows (1):

$$HI = \frac{PCE_{reverse} - PCE_{forward}}{PCE_{reverse}} \quad (1)$$

This article is protected by copyright. All rights reserved.

Author Manuscript

where $PCE_{reverse}$ and $PCE_{forward}$ represent the PCE values for the reverse and forward scans, respectively (Table S2, Supporting Information). As the scan rate decreases, the magnitude of hysteresis increases regardless of the interfacial treatment. The maximum hysteresis will be observed at scan rates below 80 mV/s, particularly at very slow rates. However, when comparing with ref-SnO_2 samples, the interfacial treatments (PEIE and mixed treatment) lead to a significant decrease in hysteresis magnitude at all scan rates. According to the previous paper, the hysteresis can be reduced by lowering the defect densities and recombination rates.[42] As a result, the interfacial treatments effectively reduce defect densities and recombination rates, leading to the suppression of ion motion as compared to ref-SnO_2.

After optimizing the PSC, we fabricated a PSK-based photoanode. To prevent moisture-induced performance deterioration of the PSK, a Ni foil was inserted as an encapsulating metal (Figure 1a). To ensure an efficient conduction between the Ni foil and the Au layer (electrode), several electrically conducting materials including silver paste, Ga–In eutectic liquid metal, silver epoxy, and carbon powder were employed. The application

This article is protected by copyright. All rights reserved.

Author Manuscript

of these conducting materials, except the carbon powder, changed the color of the PSK anode to gray, indicating that liquid phase-based materials can penetrate and damage perovskite films (Figure S4, Supporting Information). This result suggests that a solvent-free carbon powder is the optimal electrical conductor for PSK photoanodes. The PEC performances of the three different photoanodes, viz. (ITO/SnO_2/PSK/spiro-OMeTAD/Au/carbon powder/Ni foil) w/ref-SnO_2, w/PEIE-SnO_2, and w/mixed-SnO_2, were characterized by linear sweep voltammetry (LSV) under 1-sun illumination (Figure 1c). The PEC performance correlates well with the PV performance according to different interface treatments on SnO_2. Especially, the photoanode w/mixed-SnO_2 exhibits the highest current density of 19.7 mA cm^{-2} at 1.23 V_{RHE} with a slightly enhanced onset potential of 0.5 V_{RHE}; these values are improved compared with those shown by the photoanodes w/ref-SnO_2 and w/PEIE-SnO_2. Compared to PSC, the fill factor loss was observed. In PEC device, the photogenerated carriers must participate in an additional electrochemical reaction at electrode (catalyst)/electrolyte interface. Especially, OER exhibits sluggish kinetics involving a four-electron-transfer reaction, leading to a drastic fill factor loss. To confirm the stable operation of the PSK photoanode without any damage, the stability of the device was

This article is protected by copyright. All rights reserved.

Author Manuscript

analyzed in 1 M KOH (pH 14; electrolyte) at 1.23 V_{RHE} under continuous simulated 1-sun illumination. The photoanode w/ref-SnO_2 operated only for 12 h, while retaining ~50 % of its initial current density, and then exhibited a steep performance degradation. In contrast, the photoanodes w/PEIE-SnO_2 and w/mixed-SnO_2 demonstrated longer stable operations. The most remarkable stability improvement was observed in the photoanode w/mixed-SnO_2, which maintained over 60% of its initial current density for 42 h. To the best of our knowledge, the photoanode w/mixed-SnO_2 exhibited the durable operational stability compared with the previously reported PSK photoelectrodes (Table S3, Supporting Information). Without encapsulation, however, PSC showed a steep decrease of ~25% from its initial current density within 3 h under continuous operation at short circuit condition owing to various external stimuli (*e.g.*, air, light, heat, or moisture) (Figure S5, Supporting Information). It is well known that the PSK material is vulnerable to the oxygen and moisture exposure. As shown in Figure S6 (Supporting Information), the PSK layer showed no changes when immersed in DI water or exposed to air because thick Ni-foil encapsulation completely prevented oxygen and water permeation into PEC photoanode. We also observed that the PSK photoanode remained unchanged in X-ray diffraction (XRD)

This article is protected by copyright. All rights reserved.

Author Manuscript

and photoluminescence (PL) results after immersion in DI water or exposure to air for more than 80 h, which exceeds the operation time (Figure S7, Supporting Information). Additionally, we conducted the measurements of the PEC performance after immersion in DI water or exposure to air, and negligible changes were observed (Figure S8**,** Supporting Information). Hence, we concluded that the effects of oxygen and moisture on the degradation of the photoanode can be excluded. We obtained time-lapse images of the PSK photoanodes during chronoamperometry measurements to confirm the degradation during the PEC operation. As depicted in Figure S9 (Supporting Information), the degradation of the PSK photoanode is revealed by the gradually decomposing PSK layer. When the PSK layer completely disappears underneath the active area, the device shows a steep deterioration. Excluding the effects of oxygen, moisture, and heat from light, the PSK photoanode degradation can be attributed to an excess carrier accumulation at the SnO_2/PSK interface, which in turn accelerates the phase separation of the perovskite.[43, 44] We performed XRD and PL measurements on ref and mixed-SnO_2 photoanode after stability test of PSK photoanode at 1.23 V_{RHE} under 1 sun illumination. In the XRD spectra of the ref-SnO_2 sample, we observed a peak shift of the (100) plane and the presence of

This article is protected by copyright. All rights reserved.

Author Manuscript

PbI_2 phase (Figure S10a, Supporting Information). However, in mixed-SnO_2 condition, the peak shift of (100) plane and PbI_2 peak ratio were lessened than ref-SnO_2 sample. This result indicates that interfacial treatment can suppress the PbI_2 segregation and retard the degradation. Additionally, in the PL analysis, the mixed-SnO_2 showed a smaller PL peak shift to higher wavelength than the ref-SnO_2 (Figure S10b). The red-shift of PL peak is attributed to iodine ion migration, leading to phase separation and degradation.[45] Time-of-flight secondary ion mass spectrometry (TOF-SIMS) further confirmed the perovskite degradation, revealing a pronounced distribution of I ions towards the hole-transport layer (HTL) in the ref-SnO_2 (Figure S11, Supporting Information). This result suggests that iodide migration is the main cause of degradation, which can be mitigated through interfacial treatment.[46] According to previous studies, unextracted excess electrons are considered as a major factor to this iodine migration-induced degradation. Moreover, iodine vacancy has the lowest activation energy for migration as compared to other ions, making it more likely to migrate to the electron-accumulated interface such as ETL [43, 47] As a result, iodine ion migrates towards the HTL and reacts with hole, leading to the formation of PbI_2 and degradation of the perovskite. Based on a comprehensive analysis of experimental results

This article is protected by copyright. All rights reserved.

Author Manuscript

and previous literature, iodine ion migration appears to be the primary cause of degradation.

X-ray photoelectron spectroscopy (XPS) was carried out to identify interface-treatment-induced changes in the surface chemical states of SnO_2. For the XPS analysis, three different samples were prepared: ITO/ref-SnO_2 (without any interface treatment), ITO/PEIE-SnO_2, and ITO/mixed-SnO_2. The observation of the Cl 2p and N 1s XPS peaks confirm the successful deposition of the PEIE and CBSA molecules on SnO_2 (Figure S12, Supporting Information). In the spectra of the ref-SnO_2 sample, the Sn $3d_{3/2}$ and Sn $3d_{5/2}$ peaks are located at 486.7 and 495.2 eV, respectively (**Figure 2a**).[48] Upon the decoration of PEIE on SnO_2, the resulting Sn peak positions are nearly identical with those of the ref-SnO_2 sample. In contrast to the ref-SnO_2 sample spectrum, the Sn peak in the spectrum of the mixed-SnO_2 sample shifts toward the higher binding energy side by approximately 0.4 eV, which is indicative of increased Sn oxidation states on the surface. It has been reported that the oxygen vacancy (V_O) and hydroxyl group on SnO_2 represent typical surface defects, which generate unsaturated dangling bonds that trap electrons and thus hinder charge

This article is protected by copyright. All rights reserved.

Author Manuscript

transport.[49] To observe the interface treatment dependence of the surface chemical changes, the O 1s XPS spectra were recorded as shown in Figure 2b–d. Here, all the O 1s peaks are deconvoluted at 530.8 and 531.5 eV, which originate from the Sn–O bonds and from the oxygen vacancies or absorbed hydroxyl groups, respectively.[38, 50, 51] For ref-SnO_2, the peak area fraction of (V_O + hydroxyl group) with respect to that of (O_{all}) is 0.51 (Table S4, Supporting Information). In contrast to the untreated ref-SnO_2 sample, the PEIE treatment induces an insignificant change in the fraction of (V_O + hydroxyl group) in the spectra of the treated samples. This observation indicates that the PEIE polyelectrolyte-based dipole layer does not passivate V_O and the hydroxyl groups. Conversely, the peak area fraction of (V_O + hydroxyl group) in the XPS spectrum of the mixed-SnO_2 sample significantly decreases to 0.35, implying that the SO_3H functional group in CBSA self-assembles on SnO_2 and passivates the surface oxygen defects.[38] The reduced surface defects likely facilitate carrier extraction while minimizing the electron trapping or accumulation at the SnO_2/PSK interface. XRD analyses were also performed to confirm the crystallinity of the PSK films deposited on top of SnO_2 after different interface treatments. The photoanodes show nearly identical XRD peaks irrespective of the PEIE and mixed

This article is protected by copyright. All rights reserved.

Author Manuscript

PEIE+CSBA treatment, suggesting that the interface treatment does not alter the PSK crystallinity (Figure S13, Supporting Information). Scanning electron microscopy (SEM) analyses reveal that all the PSK films have similar morphologies and film thicknesses (Figure S14, Supporting Information). Therefore, it can be concluded that both the PEIE and mixed treatments only affect the electronic properties of SnO_2.

Kelvin probe force microscopy (KPFM) was used to evaluate the interface-treatment-dependence of the surface energy band of SnO_2. The work function of both PEIE and mixed (PEIE+CBSA)-SnO_2 drastically decreases to 4.3 eV compared to that of ref-SnO_2 (4.7 eV) (Figure S15, Supporting Information). This result indicates that both interfacial treatments induce an upward shift of the SnO_2 band energy and reduce the band offset between PSK and SnO_2, eventually leading to a more efficient carrier extraction than ref-SnO_2 (Figure S16, Supporting Information). Interestingly, the mixed-SnO_2 condition shows better performance than PEIE-SnO_2. Topography and current maps obtained by conductive atomic force microscopy (c-AFM) are shown in Figure 2e and f, respectively. All the three samples (ref-SnO_2, PEIE-SnO_2, and mixed-SnO_2) reveal almost identical surface topographies and roughness. The presence of the PEIE and mixed (PEIE+CSBA) layers cause only negligible

This article is protected by copyright. All rights reserved.

changes in the morphology of SnO_2 as confirmed by the SEM results (Figure S14). The root-mean-square roughness (R_q) for each condition is almost identical, indicating that the interface treatment (either PEIE or mixture of PEIE+CBSA) conformally decorates SnO_2. However, in the current mapping images measured at 0.2 V, both ref-SnO_2 (I_{avg} = 12 pA) and PEIE-SnO_2 (I_{avg} = 22 pA) exhibit small current values. This implies that the carriers have to tunnel through PEIE due to its large bandgap energy (6.2 eV) and insulating nature.[36, 37] By contrast, mixed-SnO_2 shows a much higher I_{avg} of 93 pA, which is four-fold higher than that of PEIE-SnO_2. This observation suggests that the conductivity of SnO_2 is enhanced by the conjugated CBSA molecule, which is capable of promoting charge transport at the SnO_2/PSK interface. To confirm the charge transport between SnO_2 and PSK at the interface, we deposited a PSK film on top of each SnO_2 ETL. As shown in Figure S17 (Supporting Information), the current distribution of mixed-SnO_2/PSK is higher than those of PEIE-SnO_2/PSK and ref-SnO_2/PSK samples. According to previous density functional theory-based studies, the Cl functional group in CBSA can effectively passivate the iodine vacancy in PSK.[39] Consequently, the defects at the interfaces of both the SnO_2 and PSK sides are readily passivated by the conjugated CBSA molecule, which acts as a conductive passivator at the

Author Manuscript

This article is protected by copyright. All rights reserved.

Author Manuscript

SnO_2/PSK interface. As a result, we conclude that the mixed treatment exhibits synergistic effects, including proper band alignment, defect passivation, and conductivity enhancement, which leads to an improved charge extraction.

The influence of interface engineering on the carrier dynamic was characterized by steady-state PL measurements (**Figure 3a**). The emission peak at approximately 790 nm appears in the PL spectra of all the PSK films. However, the intensity of this PL emission from the mixed-SnO_2/PSK film is remarkably lower than that of the PL peak emitted by ref-SnO_2/PSK. This result suggests carrier transport enhancement in the mixed-SnO_2/PSK film owing to the synergistic effects of the mixed PEIE+CBSA treatment.[52] Next, space charge-limited current (SCLC) analysis of the glass/ITO/SnO_2/PSK film/Au device was performed to evaluate the trap states in the PSK device (Figure S18, Supporting Information). The observed three linear regions can be defined as the ohmic, trap-filled, and child regions. At low voltages, the current is linearly proportional to the voltage in the ohmic region. At intermediate voltages, the current exponentially increases in the trap-filling region.[53–55] The V_{TFL} values of ref-SnO_2, PEIE-SnO_2 and mixed-SnO_2 are determined

This article is protected by copyright. All rights reserved.

Author Manuscript

to be 1.1, 0.8, and 0.39 V, respectively. Furthermore, we employed the pulsed voltage-SCLC method to minimize the influence of mobile ions in PSK during SCLC measurement (Figure S19, Supporting Information).[56] We applied the pre-bias of 5 V for 4 min followed by immediate SCLC measurement. The 4-min pulse applying reduced hysteresis as compared to no pulse condition, indicating that pre-bias application reduces the influence of mobile ions (Figure S20, Supporting Information). As shown in Figure S20, the trap-filled limit voltage (V_{TFL}) values of ref-SnO_2, PEIE-SnO_2 and mixed-SnO_2 are determined to be 0.92, 0.71, and 0.42 V, respectively. The mixed -SnO_2 showed the lowest V_{TFL} value in pulsed voltage-SCLC, which is the identical inclination without applying pre-bias in Figure S18. This result obviously indicated that the number of trap states at the SnO_2/PSK interface decreases, facilitating an enhanced carrier extraction, which well matched with XPS and PL results. To further investigate the trap states at the SnO_2/PSK interface, time-resolved photoluminescence (TRPL) measurements were conducted (Figure S21). A double exponential decay function was used to fit the TRPL spectra, and the obtained fitting results are listed in Table S5 (Supporting Information). The carrier lifetimes are found to be in the order of mixed-SnO_2/PSK (τ_{ave} = 24.4 ns) < PEIE-SnO_2/PSK (τ_{ave} = 59.2 ns) < ref-SnO_2/PSK

This article is protected by copyright. All rights reserved.

(τ_{ave} = 101.5 ns). This observation is consistent with the steady-state PL and SCLC analyses results, which indicate carrier extraction enhancement at the SnO_2/PSK interface in the mixed-SnO_2 sample.[38]

Notably, the PL and TRPL analyses only reveal the carrier dynamics for radiative recombination processes in the PSK absorber after photoexcitation.[57] Thus, it is necessary to investigate the ultrafast carrier dynamics, including photocarrier separation and non-radiative recombination, which were evaluated by transient absorption spectroscopy (TAS) in this study.[38, 57, 58] Continuous 2D pseudo-color spectra obtained as functions of time delay and probe wavelength under different interface treatments are presented in Figure S22 (Supporting Information). The negative signal around 740 nm can be denoted as the ground state bleaching (GSB) signal, which can be attributed to the charge depletion of the valence band of PSK. The corresponding TA spectra are shown as functions of wavelength and various pump-probe time delays in Figure S23 (Supporting Information). All the three TA spectra exhibit similar features showing one GSB peak at ~740 nm. However, the GSB peaks of PEIE-SnO_2 and mixed-SnO_2 are slightly shifted toward higher

Author Manuscript

This article is protected by copyright. All rights reserved.

Author Manuscript

wavelengths (*i.e.*, 742 nm) compared to that of ref-SnO_2 (*i.e.*, 737 nm). This observation indicates that the interface treatment enables a proper adjustment of the band alignment between PSK and SnO_2, consistent with the KPFM results (Figure S15). For a quantitative analysis of the photocarrier dynamics, the time constants are extracted from the GSB peak of each SnO_2 ETL, and the obtained decay curves of the three samples are fitted with a double exponential decay function. The corresponding fitting results are presented in Figure 3b and Table S6 (Supporting Information). Reportedly, a faster time constant (τ_1) plausibly stems from the extraction of electrons from the PSK absorber layer to the SnO_2 conduction band, whereas a slower time constant (τ_2) represents excited-state decay via non-radiative recombination at the trap states and grain boundaries within the PSK absorber.[57, 59] The τ_1 values of ref-SnO_2, PEIE-SnO_2, and mixed-SnO_2 are estimated to be 513, 241, and 98 ps, respectively. The faster time constant for the mixed-SnO_2 GSB peak is significantly reduced to nearly six and three times shorter than those for ref-SnO_2 and PEIE-SnO_2, respectively. This result implies that the electron accumulation at the SnO_2/PSK interface is effectively suppressed by the interface treatment with PEIE+CSBA. In contrast, the slower time constants (τ_2) for the PEIE-SnO_2 and mixed-SnO_2 samples are slightly

This article is protected by copyright. All rights reserved.

Author Manuscript

decreased compared to that for ref-SnO_2, indicating that non-radiative recombination within PSK is alleviated upon the interface treatment. Thus, it can be concluded that the combined use of PEIE and CSBA enables carrier extraction at the SnO_2/PSK interface, presumably leading to an efficient and hysteresis-free PSK device.

Three different PSK photoanodes (*i.e.*, ITO/SnO_2/PSK/spiro-OMeTAD/Au/carbon powder/Ni foil) based on w/ref-SnO_2, w/PEIE-SnO_2, and w/mixed-SnO_2 were fabricated. Photoelectrochemical impedance spectroscopy (PEIS) was performed in the frequency range of 300 kHz to 0.1 Hz under 1-sun illumination at the onset potential of 0.5 V_{RHE}. The Nyquist and bode plots are shown in Figure 3c and Figure S24 (Supporting Information). The arcs are fitted according to a Randles circuit model consisting of a series resistance (R_s) and a charge transfer resistance (R_{ct}), as indicated in the inset of Figure 3c. The arc radius decreased in the order of ref-SnO_2 > PEIE-SnO_2 > mixed-SnO_2 and the fitted impedance spectra were summarized in Table S7. A slight increase in high-frequency resistance was observed in the case of the mixed SnO_2 sample (Table S7, Supporting Information). High frequency region is influenced by artifacts including interference by the

This article is protected by copyright. All rights reserved.

Author Manuscript

reference electrode and ohmic resistances by electrolyte, contacts, and wires. These artifacts have no direct relevance for the semiconductor junctions.[60, 61] We anticipate that this could be due to additional resistance introduced during the electrical connection process between the substrate and the electrode for photoanode fabrication. However, in the impedance spectra, it is evident that the difference between mid and low-frequency resistance depending on the interfacial treatment is more dominant as compared to the resistance variations caused by the artifacts (Figure 3c). Therefore, the impact of series resistance change on the performance would be minimal (Table S7). The lower R_{ct} value for mixed-SnO_2 photoanode as compared to the ref-SnO_2, and PEIE-SnO_2 photoanodes indicates that more charge carriers are extracted to the electrolyte. This is attributed to the result that the charge carriers are transported to the photoanode/electrolyte interface without recombination loss through mixed treatment, which is consistent with TAS and PL results.

Transient photocurrent analysis (TPC) of the three PSK photoanodes was also performed to gain further insights into the charge accumulation phenomenon that occurs

This article is protected by copyright. All rights reserved.

Author Manuscript

during the PEC operation. Interestingly, after the initial decay of the positive current, the three devices exhibit a negative current irrespective of the interface treatment. The observed cathodic current can be attributed to a reverse charge flow within the PSK photoanode owing to charge accumulation.[62, 63] As shown in Figure 3d, the charge accumulation is remarkably alleviated in the order of w/ref-SnO_2 < w/PEIE-SnO_2 < w/mixed-SnO_2. The PEIS and TPC analyses confirmed that the mixed PEIE+CSBA treatment on SnO_2 facilitates an effective extraction of charge carriers at the interface during the PEC operation, in good agreement with the TAS result. In particular, the mixed PEIE+CSBA treatment significantly retards the PSK decomposition during the PEC operation. According to a previous study, the accumulated excess electrons promote halide migration.[43] Owing to the electron accumulation at the ETL/PSK interface, the mobile iodide ions migrate toward the HTL side, resulting in the oxidation of the iodide ions by the photogenerated holes; this process induces the formation of neutral iodine and an irreversible perovskite decomposition.[64] Therefore, it can be concluded that the mixed PEIE+CSBA treatment on SnO_2 effectively suppresses the migration of iodide anions, resulting in a high-performance and stable PSK photoanode.[43, 44]

This article is protected by copyright. All rights reserved.

Author Manuscript

Since the Ni foil has a low OER catalytic activity, hydrothermally synthesized NiFe layered double hydroxide (NiFe-LDH) on Ni foam (denoted as NiFe-LDH@Ni foam) was employed as an OER co-catalyst, followed by attachment of NiFe-LDH@Ni foam onto the Ni foil of the PSK photoanode (*i.e.*, ITO/mixed-SnO_2/PSK/spiro-OMeTAD/Au/carbon powder/Ni foil/NiFe-LDH@Ni foam, Figure S25, Supporting Information) (see Experimental section for further details).[65] The champion OER performance of the PSK photoanode with the NiFe-LDH@Ni foam catalyst was characterized by LSV under 1-sun illumination in 1 M KOH. As evident from the LSV graph in **Figure 4a**, the performance of the PSK/Ni foil/NiFe-LDH@Ni foam device is significantly improved compared to that of the device with the PSK photoanode w/mixed-SnO_2 (Figure 1c). In particular, the onset potential is decreased to 0.34 V_{RHE}, and the saturation current is 22.7 mA cm^{-2} at 0.7 V_{RHE}, indicating that the NiFe-LDH@Ni foam acts as an OER catalyst. The crystallinity and chemical state of the NiFe-LDH@Ni foam catalyst were investigated by XRD and XPS (Figure S26 and 27, Supporting Information). The low-intensity XRD peaks at 23°, 34.5°, and 38.5° correspond to the (006), (012), and (045) planes of NiFe-LDH, respectively. The four separate Ni 2p peaks of the NiFe-LDH@Ni foam can be ascribed to Ni $2p_{1/2}$, Ni $2p_{3/2}$, and the satellite

This article is protected by copyright. All rights reserved.

Author Manuscript

transitions, whereas the Fe 2p XPS spectra contain two peaks corresponding to Fe $2p_{1/2}$ and Fe $2p_{3/2}$ (Figure S27). The chemical state and morphology of the NiFe-LDH@Ni foam well matches with those reported previously (Figure S28, Supporting Information).[65, 66] The electrocatalytic performance of the NiFe-LDH@Ni foam was evaluated in 1 M KOH in comparison to those of the bare Ni foil and Ni foam. The NiFe-LDH@Ni foam required an overpotential of only 182 mV to achieve a current density of 10 mA cm^{-2} in 1 M KOH; in contrast, the bare Ni foil (892 mV) or bare Ni foam (500 mV) required significantly higher overpotentials to achieve the same current density (Figure S29a, Supporting Information). The polarization curve shows a temporal shoulder peak of the oxidation current at 1.4 V_{RHE}, which indicates Ni oxidation reaction (Ni^{2+} to Ni^{3+}) and not OER. Moreover, the Tafel slope of the NiFe-LDH@Ni foam (72 mV/dec) is also significantly smaller than those of the bare Ni foil (719 mV/dec) and bare Ni foam (404 mV/dec) (Figure S29b). The LSV curves (Figure 4a) exhibit the pre-oxidation current at ~0.2 V_{RHE} followed by an abruptly linear current increase at 0.34 V_{RHE}. This pre-oxidation current is attributed to the Ni oxidation reaction (Ni^{2+} to Ni^{3+}) of the OER catalyst, and the OER reaction rapidly occurs beyond 0.34 V_{RHE}. At a current density of 10 mA cm^{-2}, the measured potential of the PSK/Ni foil/NiFe-LDH@Ni

This article is protected by copyright. All rights reserved.

Author Manuscript

foam photoanode (0.4 V) is different from that of the NiFe-LDH@Ni foam catalyst (1.41 V) (Figure S29c). This implies that a photovoltage of 1.01 V is developed by the PSK/Ni foil/NiFe-LDH@Ni foam photoanode, and this photovoltage value is well correlated to the V_{OC} value of the PSC w/mixed-SnO_2.[67–69] This observation indicates that despite having a multilayered structure, the device exhibits almost zero photovoltage loss. In addition, the calculated ABPE of the PSK/Ni foil/NiFe-LDH@Ni foam photoanode at 0.57 V_{RHE} is 12.9% as shown in Figure 4b. To the best of our knowledge, excluding the expensive and advanced PV-grade III–V group material-based photoanodes, the ABPE value reported here is much higher than those of the previously reported photoanodes such as $BiVO_4$, WO_3, Fe_2O_3, Sb_2S_3, perovskite-based photoanodes, Ta_3N_5, and silicon (Table S8, Supporting Information). The incident photon-to-current conversion efficiency (IPCE) of the champion PSK/Ni foil/NiFe-LDH@Ni foam photoanode measured at a low applied potential (0.45 V_{RHE}) is over 70 % in a wide visible wavelength range (Figure 4c). Moreover, the integrated photocurrent density deduced from the IPCE well matches the current density determined from the LSV curve at 0.45 V_{RHE}.

This article is protected by copyright. All rights reserved.

Author Manuscript

To evaluate the stability of the PSK/Ni foil/NiFe-LDH@Ni foam photoanode, we conducted chronoamperometry measurements at 1.23 V_{RHE} in a base electrolyte of pH 14 under continuous illumination. As evident from Figure 4d, the PSK/Ni foil/NiFe-LDH@Ni foam device operated stably, while retaining ~90% of its initial current density for 24 h and ~80 % of the initial photocurrent for 200 h. During the stable operation of the PSK/Ni foil/NiFe-LDH@Ni foam photoanode, gas chromatography was conducted to verify the occurrence of OER reaction by detecting the amount of photoelectrochemically produced O_2 gas. The quantity of the detected O_2 gas well matches with the theoretically calculated O_2 amount, indicating a Faradaic efficiency of over 90% (Figure S30, Supporting Information). Interestingly, by employing the efficient OER catalyst, the operational stability of the PSK/Ni foil/NiFe-LDH@Ni foam photoanode substantially improved, and the device showed a stable operation for over 225 h.

As the PSK/Ni foil/NiFe-LDH@Ni foam photoanode exhibited a superior performance and durability, it would be meaningful to apply the parallel illumination mode (Mode P) for an unbiased solar water splitting. As a counterpart photoelectrode, we

This article is protected by copyright. All rights reserved.

Author Manuscript

fabricated a PSK-based photocathode by simply switching the Cu wire position from the bottom to the top electrode **(Figure 5a)**. A schematic illustration of the PSK photocathode and photoanode structure was provided for clear understanding of the PSK photoelectrode (Figure S31, Supporting Information). In the PSK photocathode, the charge transfer reaction occurred at the remote bottom electrode, in which the ITO/Pt functioned as the catalyst/electrolyte interface for HER. Despite the superior performance and stability of the PSK/Ni foil/NiFe-LDH@Ni foam photoanode in 1 M KOH, SnO_2 is unstable and susceptible to reduction (Sn^{4+} to Sn) in 1 M KOH according to the Pourbaix diagram. Due to the electrolyte exposure to ITO, the PSK photocathode is easily deteriorated in a strong basic atmosphere during the HER. To achieve a stable operation and high STH efficiency, we optimized the pH and concentration of the electrolyte (Figure S32, Supporting Information). The active area (*i.e.*, catalytic interface) was fully decoupled from the absorber layer in both the PSK photoanode and photocathode so that both the charge transfer reactions (HER and OER) would occur physically remotely from the PSK absorber layers. To realize this process, we separately prepared the ITO/Pt electrode for the HER and the NiFe-LDH@Ni foam for the OER.[70] Among the various conditions, 0.5 M KPi was selected as

This article is protected by copyright. All rights reserved.

Author Manuscript

the optimum electrolyte, which showed the lowest overpotential of 1.78 V, to achieve a current density of 10 mA cm^{-2}. In Figure 5b, the champion LSV curves of the PSK/Ni foil/NiFe-LDH@Ni foam photoanode and PSK/Pt photocathode in 0.5 M KPi are overlapped to determine the maximum operation point of the PSK-based Mode P-configured device; the curves intersect at 17.3 mA cm^{-2} at 0.8 V_{RHE}, and owing to parallel configuration, the expected operating current is halved to 8.65 mA cm^{-2}. The actual operating performance of the PSK Mode P-configured photoelectrode was characterized using a two-electrode configuration under 1-sun dual illumination on both the PSK photoanode and photocathode; the scanning was performed from -0.6 V to 0.6 V (Figure 5c). The Mode P-configured photoelectrode exhibits a current density of 8.84 mA cm^{-2} at 0 V (unbiased condition) in 0.5 M KPi; and this value is close to the estimated operation current density. Moreover, compared with the *J–V* curve of the PSK photoanode in 0.5 M KPi (Figure 5c), that of the PSK Mode P-configured photoelectrode demonstrates an approximately 1 V anodic shift, which is induced by the PSK/Pt photocathode. This implies that the PSK photocathode provides a 1 V photovoltage for the unbiased solar water splitting, consistent with the V_{OC} value of the PSC w/mixed-SnO_2.[71] This operational current

This article is protected by copyright. All rights reserved.

Author Manuscript

corresponds to an STH efficiency of 10.9%, which is superior to that of the $BiVO_4$-based tandem configuration (Table S9, Supporting Information). The chronoamperometry analysis of the PSK Mode P-configured unbiased photoelectrode was performed under continuous illumination to determine the long-term stability, and the corresponding results are shown in Figure 5d. Evidently, the PSK Mode P cell retains 70% its initial current density after 22 h. The Faradaic efficiency was determined by gas chromatography to measure the amount of H_2 gas produced during the PEC reaction without any side reaction. The measured quantity of the H_2 gas is consistent with that estimated theoretically, revealing an approximately 90–100% Faradaic efficiency (Figure S33, Supporting Information). The operational stability of the PSK Mode P-configured unbiased photoelectrode is poorer than that of a single electrode of the PSK/Ni foil/NiFe-LDH@Ni foam photoanode in 1 M KOH. After the Mode P device deterioration, we tested the PEC performance of the PSK/Ni foil/NiFe-LDH@Ni foam photoanode and detected only a slight decrease in the photocurrent density (Figure S34, Supporting Information). By contrast, the PSK/Pt photocathode underwent a complete degradation, implying that the deterioration of the Mode P-configured unbiased photoelectrode originates from the PSK/Pt photocathode.

This article is protected by copyright. All rights reserved.

Author Manuscript

We speculate that the electrons need to travel a long path (SnO_2 → ITO → Pt, in Figure S31) in the PSK photocathode to reach the remote Pt/electrolyte interface for HER. Thus, the current PSK photocathode configuration is vulnerable to electron accumulation at the SnO_2/ITO interface and thus undergoes a rapid degradation compared to the PSK photoanode. Further studies focused on the development of more efficient PSK photocathode structures (p-i-n) are required to minimize the electron travel pathway for HER.

3. Conclusions

We introduced a simple and effective interface engineering to improve the performance and stability of PSK photoanodes by decorating the SnO_2/PSK interface with a mixture of PEIE and CBSA. The mixed PEIE+CBSA treatment effectively passivated the surface defects of SnO_2 as well as enhanced its conductivity, while favorably aligning the energy bands between SnO_2 and PSK, thereby facilitating carrier extraction at the SnO_2/PSK interface. As a result, the V_{OC} and J_{SC} of the PSC w/mixed-SnO_2 were enhanced, and the PSK photoanode

This article is protected by copyright. All rights reserved.

Author Manuscript

w/mixed-SnO_2 exhibited an onset potential of 0.34 V_{RHE}, a saturated photocurrent density of 22.7 mA cm^{-2} at 0.7 V_{RHE}, and a superior ABPE of 12.9% at 0.57 V_{RHE}. Furthermore, the PSK photoanode exhibited an outstanding durability for 225 h, while maintaining ~70 % of the initial photocurrent at 1.23 V_{RHE} under continuous illumination. The w/mixed-SnO_2 sample exhibited a record high onset potential, performance, and stability, which surpassed those of the other previously reported PSK-based photoanodes. By coupling the photoanode with an inverted-type PSK photocathode, a bias-free solar water splitting was successfully achieved with a noticeable efficiency (~10.9%). This interface engineering strategy is easily processable, reproducible, and effective at an ETL/PSK interface. Our work establishes a new benchmark for efficient and stable PSK photoelectrodes for PEC water splitting.

4. Experimental Section

Materials: Methylammonium iodide (MAI), formamidinium iodide (FAI), and methylammonium bromide (MABr) were purchased from Greatcell Solar (Queanbeyan,

This article is protected by copyright. All rights reserved.

Author Manuscript

Australia). Lead(II) iodide (PbI_2 beads, metal basis), and SnO_2 colloid (tin(IV) oxide, colloidal dispersion 15% in H_2O) were purchased from Alfa Aesar (Ward Hill, MA, USA). Lead bromide ($PbBr_2$, 99.999%), cesium iodide (CsI, 99.999%, trace metal basis), acetonitrile (anhydrous, 99.8%), dimethylformamide (anhydrous, 99.8%), chlorobenzene (anhydrous, 99.8%), dimethylsulfoxide (anhydrous, 99.8%), 80% ethoxylated polyethyleneimine, 4-tert-butylpyridin (TBP, 96%), 2,2′,7,7′-tetrakis(N,N-dip-methoxyphenylamin-9,9′-spirobifluorene (spiro-OMeTAD), 4-chlorobenzene sulfonic acid (CBSA, 98%) and bis(trifluoromethane) sulfonimide lithium salt (Li-TFSI, 99.95%) were purchased from Sigma–Aldrich (St. Louis, MO, USA). All the chemical materials were used in the as-received conditions without any modification.

Preparation of ETLs: The ETL precursor was prepared by diluting an SnO_2 colloid dispersion (Alfa Aesar) with deionized (DI) water (1:4 volume ratio), followed by stirring for 30 min. The ITO substrate was first patterned by laser etching (Korthem Science, Korea) and then cleaned through sequential sonication with DI water, ethanol, and acetone for 15 min (for each cleaning agent). After the cleaning process, ultraviolet treatment was

This article is protected by copyright. All rights reserved.

Author Manuscript

performed for 15 min. The diluted SnO_2 colloid dispersion was spin-coated on the cleaned ITO glass at 3000 rpm for 30 s, and the coated glass was subsequently annealed at 150 °C for 30 min. To fabricate the PEIE-modified SnO_2, an 80% ethoxylated polyethyleneimine solution was diluted with DI water (0.025 wt%). The diluted PEIE solution was spin-coated on ITO/SnO_2 at 5000 rpm for 20 s, followed by drying at 100 °C for 5 min. To prepare the mixed-SnO_2, CBSA was additionally dissolved in the diluted PEIE solution to adjust the concentration to 10 mM, and the mixed solution was sonicated for 30 min. After the sonication, the mixed solution was spin-coated onto ITO/SnO_2 at 5000 rpm for 20 s, followed by drying at 100 °C for 5 min.

Fabrication of the PSK photoanode and photocathode: The perovskite precursor was prepared by mixing 223.56 mg of FAI, 29.1 mg of MABr, 653.25 mg of PbI_2, and 104.1 mg of $PbBr_2$ in a solvent mixture of dimethylformamide (DMF; 0.9 mL) and dimethyl sulfoxide (DMSO; 0.1 mL). Subsequently, 40 µL of a CsI solution (506.63 mg in 1 mL DMSO) was added to the precursor and stirred for 1 h. The solution was spin-coated on the as-prepared SnO_2 substrate at 1200 rpm for 12 s, followed by a re-coating at 5800 rpm for

This article is protected by copyright. All rights reserved.

Author Manuscript

20 s. The twice-spin-coated SnO_2 substrate was then annealed at 100 °C for 1 h. Next, 72 mg of spiro-OMeTAD, 28.8 µL of TBP, and 17.5 µL of an Li-TFSI solution (520 mg of Li-TFSI in 1 mL of acetonitrile) were dissolved in 1 mL of chlorobenzene, and the resulting solution was spin-coated on the fabricated perovskite films at 3000 rpm for 30 s to form the HTL. Next, an 80-nm-thick Au top electrode was thermally evaporated on the HTL. Conductive carbon powder (Ketjen) and epoxy (Henkel, LOCTITE 120 HP) were then spread on the Au layer, followed by attaching a Ni foil (0.125 mm, Sigma Aldrich). Prior to attaching with the Au layer, the Ni foil was cleaned through sequential sonication with DI water, ethanol, and acetone for 15 min (for each cleaning agent). The cleaned Ni foil was then immersed in hydrofluoric acid for 30 s to remove any surface oxide. After the Ni foil attachment, an epoxy resin was used for encapsulating the PSK photoanode, except the active area, for preventing water permeation. To introduce the OER catalyst, a Ni–Fe layered double hydroxide was synthesized on the Ni foam by the hydrothermal method. The Ni foam was also cleaned through sequential sonication with DI water, ethanol, and acetone for 15 min (for each cleaning agent). The surface-cleaned Ni foam was then immersed in 3 M HCl and sonicated for 15 min to remove the native oxide. Next, 0.3 g of

This article is protected by copyright. All rights reserved.

Author Manuscript

($Ni(NO_3)_2·6H_2O$), 0.6 g of $CO(NH_2)_2$, and 0.38 g of $Fe(NO_3)_3·9H_2O$ were dissolved in 70 mL DI water under sonication for 15 min. The hydrothermal reaction was conducted for 10 h at 110 °C inside a 100 mL Teflon-lined stainless-steel autoclave, inside which the cleaned Ni foam was submerged into the precursor solution. The resultant sample was ultrasonically washed several times by DI water for removing the residual reactants and then dried at 80 °C for 12 h in air. The as-prepared NiFe-LDH@Ni foam was attached to the Ni foil (active area) using a silver paste (Elcoat). On the PSK photocathode, a Cu tape was attached to the Au region, and then a Cu wire was attached as well. The Pt catalyst was deposited on the active area by using a 108 Auto Sputter Coater (Ted Pella, Redding, CA, USA), which was operated for 120 s under 0.1 mbar of Ar atmosphere and a current of 10 mA.

Optical, structural, and electrical property characterizations: Field-emission SEM (JSM-7001F, JEOL, Japan) was employed to obtain surface and cross-sectional images. Steady-state PL graphs of the perovskite films were obtained after excitation at 532 nm (MAPLE-II, Dongwoo Optron, Korea). The SCLC measurements were conducted using a Keithley 2400 source meter (Keithley Instruments Inc., Cleveland, OH, USA) under dark

This article is protected by copyright. All rights reserved.

Author Manuscript

conditions. Contact-mode AFM (NX-10 AFM, Park Systems, Korea) analysis was performed to observe the topology and obtain current maps of ITO/SnO_2 and ITO/SnO_2/PSK after different interface treatments. KPFM was performed under ambient conditions, after a proper tip calibration, using a freshly cleaved highly oriented pyrolytic graphite. In addition, the work function was also measured in the non-contact mode. The crystallinity of the PSK films, as a function of the differently modified SnO_2 substrates, was investigated by XRD (MiniFlex 600, Rigaku, Tokyo, Japan) using Cu K_α radiation (λ = 0.15406 nm). Furthermore, XPS (K-alpha, Thermo Scientific Inc., UK) was used to analyze the surface chemical states of the samples. All the XPS spectra were calibrated using the C 1s peak (285 eV). A Gaussian peak function was used to determine the fitted values. Ultrafast transient absorption (TA) measurements were performed at a pump fluence of 5 nJ per pulse. The laser pulse obtained from a Ti:sapphire amplifier with 1 kHz repetition rate and sub-25 fs pulse duration (LEGEND ELITE, Coherent, USA) was divided into two pulses; the strong one operated the optical parametric amplifier (TOPAS, LIGHT CONVERSION, Lithuania) at a 350 nm pump wavelength, which created photoexcited carriers in all the samples. The other pulse was passed through a nonlinear crystal to generate a white light continuum in the

This article is protected by copyright. All rights reserved.

visible wavelength range (450–780 nm) to detect differential absorption changes in the samples under a transmission geometry using a spectrometer (HELIOS, Ultrafast Systems, USA).

PV performance characterization: A solar simulator (Sol3A Class AAA, Oriel Instruments, Stratford, CT, USA) was employed to evaluate the PV performances of the PSCs under 1.5 AM and 1 sun conditions (100 mW cm^{-2}); the calibration was performed using a certified Si reference cell (Newport Corporation, Irvine, USA). The active area (0.060 cm^2) of the PSC was covered by an aperture mask and then exposed to light. Fifteen devices for each ETL condition were used for the statistical analysis. The current was measured by scanning over a range of -0.1 to 1.2 V at a rate of 0.52 V s^{-1} with a dwell time of 50 ms at each point. For the *J–V* hysteresis, the scanning was performed under identical conditions. All the PV measurements were carried out under an ambient atmosphere.

PEC measurements: Before LSV measurement, the exposed area of the PSK photoelectrodes ranged from 0.06 to 0.3 cm^2 and the catalytic area was controlled

This article is protected by copyright. All rights reserved.

Author Manuscript

Author Manuscript

to be identical with photoelectrode area. For the LSV and chronoamperometry measurements, a three-electrode system, with a Pt wire as the counter electrode and Ag/AgCl/KCl (4 M) as the reference electrode in 0.5 M KPi (pH 7), 0.1 M KOH solution (pH 14), and 1 M KOH solution (pH 14), was used under simulated solar light illumination (AM 1.5G; Newport Corporation, USA). In all PEC measurements, the wire was connected to a potentiostat (SI 1287, Solartron, UK) to control the potential and confirm the current density. Moreover, the applied potentials were calculated with respect to the RHE value for all the PEC measurements for comparison with the previously reported values; the following equation was used to calculate the applied potentials:

$$E_{RHE} = E_{Ag/AgCl} + 0.059\ pH + 0.197 \quad (2)$$

The PEIS measurements were conducted using a potentiostat with a frequency analyzer (1260, Solartron, Leicester, UK). The polarization and series resistances of the PSK photoanodes were determined in the frequency range of 300 kHz to 0.1

This article is protected by copyright. All rights reserved.

Author Manuscript

Hz at 0.5 V vs. RHE under 1-sun illumination with a 10 mV alternating-current amplitude. The IPCE and TPC measurements were performed on an electrochemical workstation (Zennium, Zahner, Germany) using a potentiostat (PP211, Zahner, Germany) and a monochromatic light source (TLS03, Zahner). Gas chromatography (6500GC system, YL Instrument, Anyang, Korea) was performed using a pulsed discharge detector and a molecular sieve column to confirm the O_2 and H_2 evolutions. Rubber bulkheads were used to seal all the connections of the PEC device completely for preventing gas leakage from the quartz.

Supporting Information

Supporting Information is available at the Wiley Online Library, or from the author.

Acknowledgements

This article is protected by copyright. All rights reserved.

This research was supported by the National R&D Program through the National Research Foundation of Korea (NRF) funded by the Ministry of Science and ICT (No. 2021R1A3B1068920 and 2021M3H4A1A03049662) and the Yonsei Signature Research Cluster Program of 2021 (2021–22–0002).

Author Manuscript

Conflict of Interest

The authors declare no conflicts of interest.

Received: ((will be filled in by the editorial staff))
Revised: ((will be filled in by the editorial staff))
Published online: ((will be filled in by the editorial staff))

References

[1] M. Gratzel, *Nature* **2001**, 414, 338.

[2] W. Yang, R. R. Prabhakar, J. Tan, S. D. Tilley, J. Moon, *Chem. Soc. Rev.* **2019**, 48, 4979.

This article is protected by copyright. All rights reserved.

Author Manuscript

[3] K. Sivula, R. van de Krol, *Nat. Rev. Mater.* **2016**, 1, 15010.

[4] C. M. Jiang, M. Farmand, C. H. Wu, Y. S. Liu, J. H. Guo, W. S. Drisdell, J. K. Cooper, I. D. Sharp, *Chem. Mater.* **2017**, 29, 3334.

[5] L. Wang, W. T. Lian, B. Liu, H. F. Lv, Y. Zhang, X. J. Wu, T. Wang, J. L. Gong, T. Chen, H. X. Xu, *Adv. Mater.* **2022**, 34, 2200723.

[6] M. Sun, R. T. Gao, J. L. He, X. H. Liu, T. Nakajima, X. Y. Zhang, L. Wang, *Angew. Chem. Int. Ed.* **2021**, 60, 17601.

[7] L. Wang, K. Marcus, X. J. Huang, Z. Q. Shen, Y. Yang, Y. P. Bi, *Small* **2019**, 15, 1970008.

[8] Y. Q. Xiao, C. Feng, J. Fu, F. Z. Wang, C. L. Li, V. F. Kunzelmann, C. M. Jiang, M. Nakabayashi, N. Shibata, I. D. Sharp, K. Domen, Y. B. Li, *Nat. Catal.* **2020**, 3, 932.

[9] Z. H. Li, L. Luo, M. Li, W. S. Chen, Y. G. Liu, J. R. Yang, S. M. Xu, H. Zhou, L. N. Ma, M. Xu, X. G. Kong, H. H. Duan, *Nat. Commun.* **2021**, 12, 6698.

[10] S. G. Shim, J. Tan, H. Lee, J. Park, J. Yun, Y. S. Park, K. Kim, J. Lee, J. Moon, *Chem. Eng. J.* **2022**, 430, 133061.

[11] S. Ye, W. W. Shi, Y. Liu, D. F. Li, H. Yin, H. B. Chi, Y. L. Luo, N. Ta, F. T. Fan, X. L. Wang, C. Li, *J. Am. Chem. Soc.* **2021**, 143, 12499.

This article is protected by copyright. All rights reserved.

Author Manuscript

[12] H. Min, D. Lee, J. Kim, G. Kim, K. S. Lee, J. Kim, M. J. Paik, Y. K. Kim, K. S. Kim, M. G. Kim, T. J. Shin, S. I. Seok, *Nature* **2021**, 598, 444.

[13] S. D. Stranks, G. E. Eperon, G. Grancini, C. Menelaou, M. J. P. Alcocer, T. Leijtens, L. M. Herz, A. Petrozza, H. J. Snaith, *Science* **2013**, 342, 341.

[14] I. S. Kim, M. J. Pellin, A. B. F. Martinson, *ACS Energy Lett.* **2019**, 4, 293.

[15] J. H. Kim, S. Seo, J. H. Lee, H. Choi, S. Kim, G. Piao, Y. R. Kim, B. Park, J. Lee, Y. Jung, H. Park, S. Lee, K. Lee, *Adv. Funct. Mater.* **2021**, 31, 2008277.

[16] E. E. Moore, V. Andrei, S. Zacarias, I. A. C. Pereira, E. Reisner, *ACS Energy Lett.* **2020**, 5, 232.

[17] R. Tao, Z. X. Sun, F. Y. Li, W. C. Fang, L. Xu, *ACS Appl. Energy Mater.* **2019**, 2, 1969.

[18] H. J. Chen, M. Zhang, T. P. Thanh, R. H. Bo, L. Shi, I. Di Bernardo, J. M. Bing, J. Pan, S. Singh, J. Lipton-Duffin, T. Wu, R. Amal, S. J. Huang, A. W. Y. Ho-Baillie, A. Tricoli, *Adv. Funct. Mater.* **2021**, 31, 2008245.

[19] P. M. Da, M. Y. Cha, L. Sun, Y. Z. Wu, Z. S. Wang, G. F. Zheng, *Nano Lett.* **2015**, 15, 3452.

[20] L. F. Gao, W. J. Luo, Y. F. Yao, Z. G. Zou, *Chem. Commun.* **2018**, 54, 11459.

[21] I. Poli, U. Hintermair, M. Regue, S. Kumar, E. V. Sackville, J. Baker, T. M. Watson, S. Eslava, P. J. Cameron, *Nat. Commun.* **2019**, 10, 2097.

This article is protected by copyright. All rights reserved.

Author Manuscript

[22] T. G. Kim, J. H. Lee, G. Hyun, S. Kim, D. H. Chun, S. Lee, G. Bae, H. S. Oh, S. Jeon, J. H. Park, *ACS Energy Lett.* **2022**, 7, 320.

[23] K. Domanski, B. Roose, T. Matsui, M. Saliba, S. H. Turren-Cruz, J. P. Correa-Baena, C. Roldan-Carmona, G. Richardson, J. M. Foster, F. De Angelis, J. M. Ball, A. Petrozza, N. Mine, M. K. Nazeeruddin, W. Tress, M. Gratzel, U. Steiner, A. Hagfeldt, A. Abate, *Energy Environ. Sci.* **2017**, 10, 604.

[24] D. A. Jacobs, C. M. Wolff, X. Y. Chin, K. Artuk, C. Ballif, Q. Jeangros, *Energy Environ. Sci.* **2022**, 15, 5324.

[25] H. C. Zhang, X. Fu, Y. Tang, H. Wang, C. F. Zhang, W. W. Yu, X. Y. Wang, Y. Zhang, M. Xiao, *Nat. Commun.* **2019**, 10, 1088.

[26] D. Di Girolamo, N. Phung, F. U. Kosasih, F. Di Giacomo, F. Matteocci, J. A. Smith, M. A. Flatken, H. Kobler, S. H. T. Cruz, A. Mattoni, L. Cina, B. Rech, A. Latini, G. Divitini, C. Ducati, A. Di Carlo, D. Dini, A. Abate, *Adv. Energy Mater.* **2020**, 10, 2000310.

[27] Z. Y. Ni, S. Xu, J. S. Huang, *Science* **2021**, 371, 1352.

[28] P. Schulz, D. Cahen, A. Kahn, *Chem. Rev.* **2019**, 119, 3349.

This article is protected by copyright. All rights reserved.

Author Manuscript

[29] Y. C. Liu, Y. X. Zhang, X. J. Zhu, J. S. Feng, I. Spanopoulos, W. J. Ke, Y. H. He, X. D. Ren, Z. Yang, F. W. Xiao, K. Zhao, M. Kanatzidis, S. Z. Liu, *Adv. Mater.* **2021**, 33, 2006010.

[30] Y. X. Zhai, K. Wang, F. Zhang, C. X. Xiao, A. H. Rose, K. Zhu, M. C. Beard, *ACS Energy Lett.* **2020**, 5, 47.

[31] L. J. Zuo, Q. Chen, N. De Marco, Y. T. Hsieh, H. J. Chen, P. Y. Sun, S. Y. Chang, H. X. Zhao, S. Q. Dong, Y. Yang, *Nano Lett.* **2017**, 17, 269.

[32] S. You, H. P. Zeng, Z. L. Ku, X. Z. Wang, Z. Wang, Y. G. Rong, Y. Zhao, X. Zheng, L. Luo, L. Li, S. J. Zhang, M. Li, X. Y. Gao, X. Li, *Adv. Mater.* **2020**, 32, 2003990.

[33] X. Gong, Q. Sun, S. S. Liu, P. Z. Liao, Y. Shen, C. Gratzel, S. M. Zakeeruddin, M. Gratzel, M. K. Wang, *Nano Lett.* **2018**, 18, 3969.

[34] H. Wang, F. B. Li, P. Wang, R. Sun, W. Ma, M. T. Chen, W. Q. Miao, D. Liu, T. Wang, *Adv. Energy Mater.* **2020**, 10, 2000615.

[35] Q. Chen, C. Wang, Y. W. Li, L. W. Chen, *J. Am. Chem. Soc.* **2020**, 142, 18281.

[36] Y. H. Zhou, C. Fuentes-Hernandez, J. Shim, J. Meyer, A. J. Giordano, H. Li, P. Winget, T. Papadopoulos, H. Cheun, J. Kim, M. Fenoll, A. Dindar, W. Haske, E. Najafabadi, T. M. Khan, H. Sojoudi, S. Barlow, S. Graham, J. L. Bredas, S. R. Marder, A. Kahn, B. Kippelen, *Science* **2012**, 336, 327.

This article is protected by copyright. All rights reserved.

Author Manuscript

[37] J. W. Yun, J. W. Tan, Y. K. Jung, W. Yang, H. Lee, S. Ma, Y. S. Park, C. U. Lee, W. Z. Niu, J. Lee, K. Kim, S. D. Tilley, A. Walsh, J. Moon, *ACS Energy Lett.* **2022**, 7, 1392.

[38] Y. Dong, W. J. Shen, W. Dong, C. Bai, J. Zhao, Y. C. Zhou, F. Z. Huang, Y. B. Cheng, J. Zhong, *Adv. Energy Mater.* **2022**, 12, 2200417.

[39] J. Q. Zhang, J. Yang, R. Y. Dai, W. P. Sheng, Y. Su, Y. Zhong, X. Li, L. C. Tan, Y. W. Chen, *Adv. Energy Mater.* **2022**, 12, 2103674.

[40] M. Saliba, T. Matsui, J. Y. Seo, K. Domanski, J. P. Correa-Baena, M. K. Nazeeruddin, S. M. Zakeeruddin, W. Tress, A. Abate, A. Hagfeldt, M. Gratzel, *Energy Environ. Sci.* **2016**, 9, 1989.

[41] T. Y. Chen, Z. Sun, M. Liang, S. Xue, *Phys. Chem. Chem. Phys.* **2020**, 22, 245.

[42] J. M. Cave, N. E. Courtier, I. A. Blakborn, T. W. Jones, D. Ghosh, K. F. Anderson, L. Y. Lin, A. A. Dijkhoff, G. J. Wilson, K. Feron, M. S. Islam, J. M. Foster, G. Richardson, A. B. Walker, *J. Appl. Phys.* **2020**, 128, 184501.

[43] Y. Z. Lin, B. Chen, Y. J. Fang, J. J. Zhao, C. X. Bao, Z. H. Yu, Y. H. Deng, P. N. Rudd, Y. F. Yan, Y. B. Yuan, J. S. Huang, *Nat. Commun.* **2018**, 9, 4981.

[44] T. A. Berhe, W. N. Su, C. H. Chen, C. J. Pan, J. H. Cheng, H. M. Chen, M. C. Tsai, L. Y. Chen, A. A. Dubale, B. J. Hwang, *Energy Environ. Sci.* **2016**, 9, 323.

This article is protected by copyright. All rights reserved.

Author Manuscript

[45] D. Di Girolamo, N. Phung, F. U. Kosasih, F. Di Giacomo, F. Matteocci, J. A. Smith, M. A. Flatken, H. Kobler, S. H. T. Cruz, A. Mattoni, L. Cina, B. Rech, A. Latini, G. Divitini, C. Ducati, A. Di Carlo, D. Dini, A. Abate, *Adv. Energy Mater.* **2020**, 10, 2000310.

[46] Y. P. Zhao, I. Yavuz, M. H. Wang, M. Weber, M. J. Xu, J. H. Lee, S. Tan, T. Y. Huang, D. Meng, R. Wang, J. J. Xue, S. J. Lee, S. H. Bae, A. Zhang, S. G. Choi, Y. F. Yin, J. Liu, T. H. Han, Y. T. Shi, H. R. Ma, W. X. Yang, Q. Y. Xing, Y. F. Zhou, P. J. Shi, S. S. Wang, E. Zhang, J. M. Bian, X. Q. Pan, N. G. Park, J. W. Lee, Y. Yang, *Nat. Mater.* **2022**, 21, 1396.

[47] C. Eames, J. M. Frost, P. R. F. Barnes, B. C. O'Regan, A. Walsh, M. S. Islam, *Nat. Commun.* **2015**, 6, 7497.

[48] J. H. Wang, H. Li, S. G. Meng, X. J. Ye, X. L. Fu, S. F. Chen, *RSC Adv.* **2017**, 7, 27024.

[49] S. Y. Park, K. Zhu, *Adv. Mater.* **2022**, 34, 2110438.

[50] H. Bi, B. B. Liu, D. M. He, L. Bai, W. Q. Wang, Z. G. Zang, J. Z. Chen, *Chem. Eng. J.* **2021**, 418, 129375.

[51] Z. Xiong, X. Chen, B. Zhang, G. O. Odunmbaku, Z. P. Ou, B. Guo, K. Yang, Z. P. Kan, S. R. Lu, S. S. Chen, N. A. N. Ouedraogo, Y. Cho, C. Yang, J. Z. Chen, K. Sun, *Adv. Mater.* **2022**, 34, 2106118.

This article is protected by copyright. All rights reserved.

Author Manuscript

[52] G. Jang, H. C. Kwon, S. Ma, S. C. Yun, H. Yang, J. Moon, *Adv. Energy Mater.* **2019**, 9, 1901719.

[53] D. Shi, V. Adinolfi, R. Comin, M. J. Yuan, E. Alarousu, A. Buin, Y. Chen, S. Hoogland, A. Rothenberger, K. Katsiev, Y. Losovyj, X. Zhang, P. A. Dowben, O. F. Mohammed, E. H. Sargent, O. M. Bakr, *Science* **2015**, 347, 519.

[54] Z. H. Liu, J. N. Hu, H. Y. Jiao, L. Li, G. H. J. Zheng, Y. H. Chen, Y. Huang, Q. Zhang, C. Shen, Q. Chen, H. P. Zhou, *Adv. Mater.* **2017**, 29, 1606774.

[55] G. Jang, S. Ma, H. C. Kwon, S. Goh, H. Ban, J. S. Kim, J. H. Kim, J. Moon, *ACS Energy Lett.* **2021**, 6, 249.

[56] E. A. Duijnstee, J. M. Ball, V. M. Le Corre, L. J. A. Koster, H. J. Snaith, J. Lim, *ACS Energy Lett.* **2020**, 5, 376.

[57] S. K. Huang, Y. C. Wang, W. C. Ke, Y. T. Kao, N. Z. She, J. X. Li, C. W. Luo, A. Yabushita, D. Y. Wang, Y. J. Chang, K. Tsukagoshi, C. W. Chen, *J. Mater. Chem. A* **2020**, 8, 23607.

[58] K. E. Knowles, M. D. Koch, J. L. Shelton, *J. Mater. Chem. C* **2018**, 6, 11853.

[59] Z. L. Zhu, J. A. Ma, Z. L. Wang, C. Mu, Z. T. Fan, L. L. Du, Y. Bai, L. Z. Fan, H. Yan, D. L. Phillips, S. H. Yang, *J. Am. Chem. Soc.* **2014**, 136, 3760.

[60] W. Yang, T. Moehl, E. Service, S. D. Tilley, *Adv. Energy Mater.* **2021**, 11, 2003569.

This article is protected by copyright. All rights reserved.

Author Manuscript

[61] H. Lee, J. W. Yang, J. Tan, J. Park, S. G. Shim, Y. S. Park, J. Yun, K. Kim, H. W. Jang, J. Moon, *Adv. Sci.* **2021**, 8, 2102458.

[62] F. Le Formal, S. R. Pendlebury, M. Cornuz, S. D. Tilley, M. Gratzel, J. R. Durrant, *J. Am. Chem. Soc.* **2014**, 136, 2564.

[63] F. Le Formal, K. Sivula, M. Gratzel, *J. Phys. Chem. C* **2012**, 116, 26707.

[64] C. C. Boyd, R. Cheacharoen, T. Leijtens, M. D. McGehee, *Chem. Rev.* **2019**, 119, 3418.

[65] Z. Qiu, C. W. Tai, G. A. Niklasson, T. Edvinsson, *Energy Environ. Sci.* **2019**, 12, 572.

[66] Z. W. Gao, J. Y. Liu, X. M. Chen, X. L. Zheng, J. Mao, H. Liu, T. Ma, L. Li, W. C. Wang, X. W. Du, *Adv. Mater.* **2019**, 31, 1804769.

[67] G. Xie, B. Guo, J. R. Gong, *Adv. Funct. Mater.* **2022**, 2210420.

[68] J. Quinn, J. Hemmerling, S. Linic, *ACS Catal.* **2018**, 8, 8545.

[69] W. Zhou, C. L. Dong, Y. Q. Wang, Y. C. Huang, L. Y. He, H. W. Chang, S. H. Shen, *Nano Res.* **2021**, 14, 2285.

[70] W. Yang, J. H. Kim, O. S. Hutter, L. J. Phillips, J. Tan, J. Park, H. Lee, J. D. Major, J. S. Lee, J. Moon, *Nat. Commun.* **2020**, 11, 861.

This article is protected by copyright. All rights reserved.

[71] H. Lee, J. W. Yang, J. Tan, J. Park, S. G. Shim, Y. S. Park, J. Yun, K. Kim, H. W. Jang, J. Moon, *Adv. Sci.* **2021**, 8, 2102458.

Author Manuscript

This article is protected by copyright. All rights reserved.

Author Manuscript

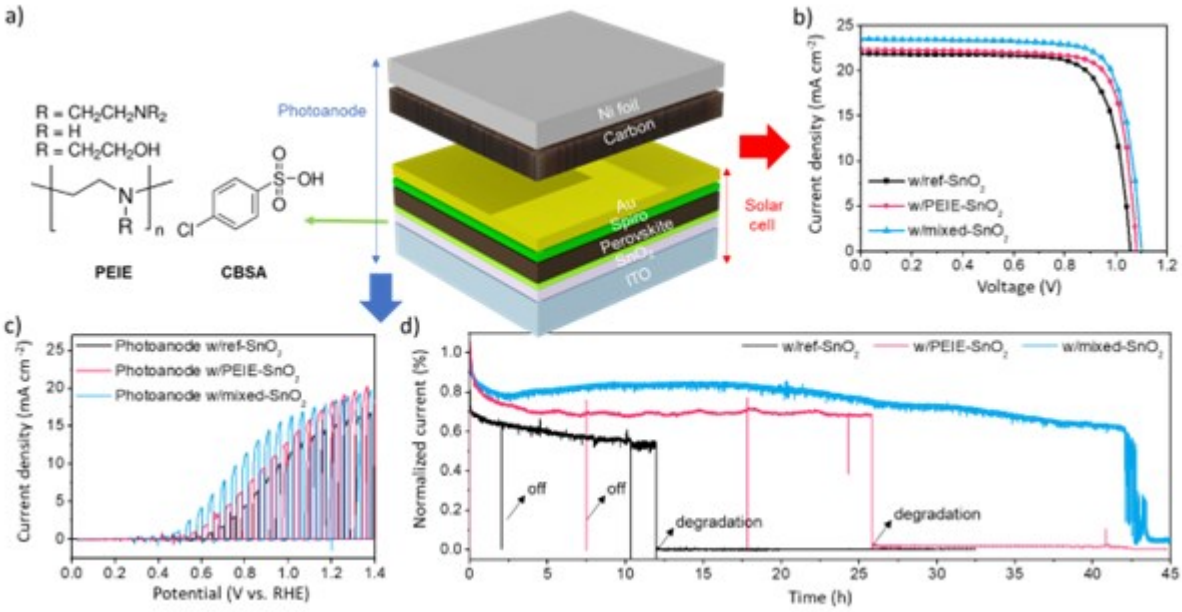
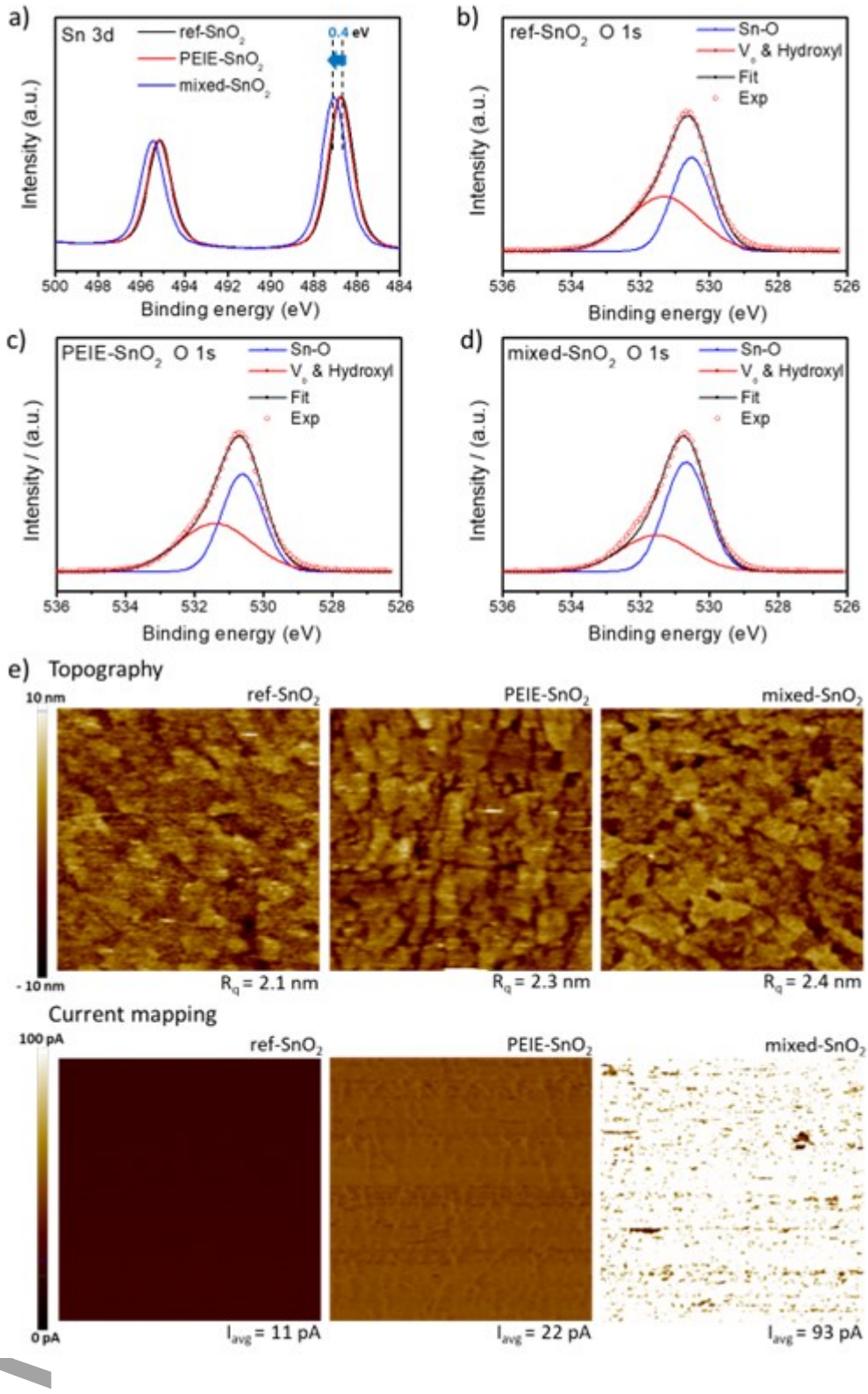


Figure 1. a) Device structure of the PSC and PSK photoanode in an ITO/SnO_2/PSK/spiro-OMeTAD/Au/carbon powder/Ni foil configuration. b) *J*–*V* curves of the champion PSCs based on w/ref-, w/PEIE-, and w/mixed-SnO_2. c) LSV curves and d) chronoamperometry results of the PSK photoanode at 1.23 V_{RHE} depending on different interface treatments (*i.e.*, ref-, PEIE-, and mixed-SnO_2); the analyses were performed under 1 sun illumination in a 1 M KOH electrolyte (pH 14).

This article is protected by copyright. All rights reserved.

Author Manuscript



This article is protected by copyright. All rights reserved.

Figure 2. XPS spectra of ITO/SnO_2 after different interface treatments (*i.e.*, ref-, PEIE-, and mixed-SnO_2): a) Sn 3d, and b-d) deconvolution of the O 1s regions. Scatter points represent the experimental results, while the solid lines represent the fitted data. e) Topography and current mapping of ref-, PEIE-, and mixed-SnO_2 determined by c-AFM.

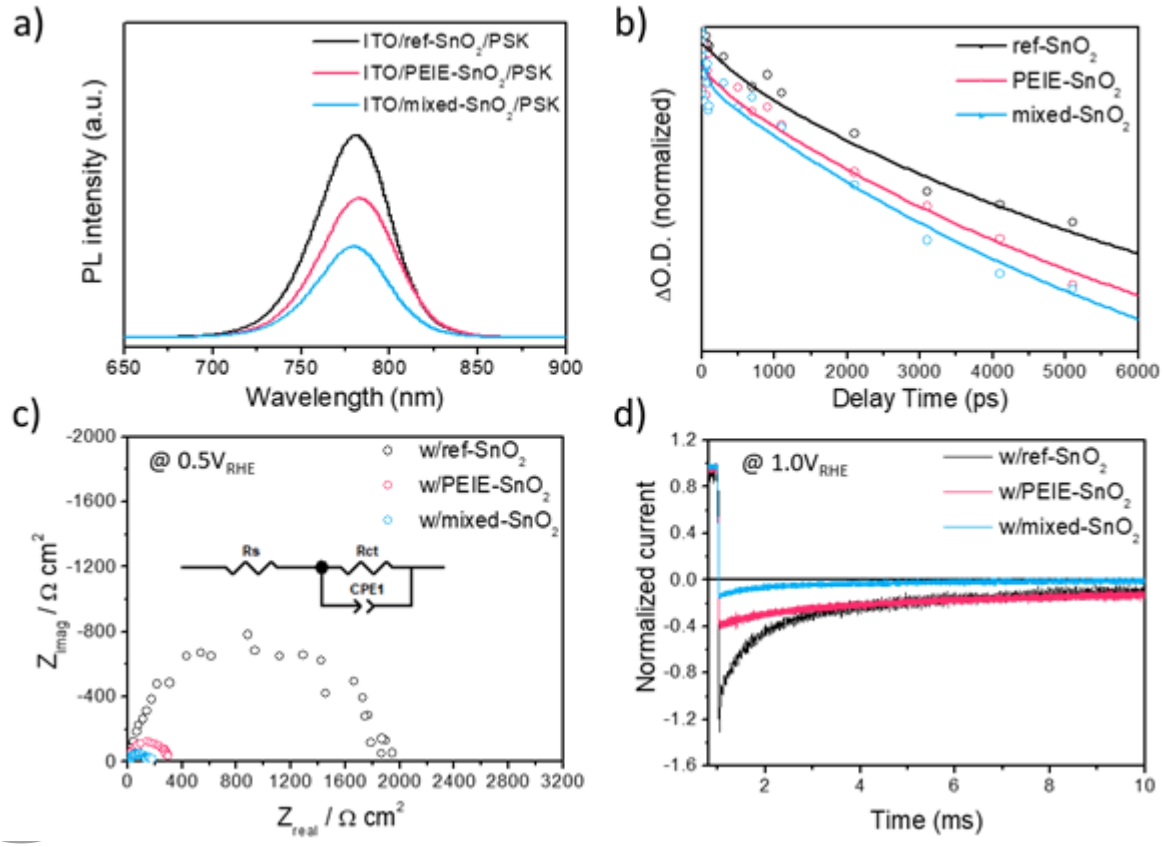


Figure 3. a) Steady-state PL of the PSK film deposited on glass/SnO_2 with different interface treatments: ref-, PEIE-, and mixed-SnO_2. b) Normalized decay traces for photobleaching obtained from the TAS spectra of ITO/SnO_2/PSK after different interface treatments (*i.e.*, ref-, PEIE-, and mixed-SnO_2). c, d) Nyquist plots and transient photocurrent curves of the

This article is protected by copyright. All rights reserved.

Author Manuscript

PSK photoanodes after different interface treatments (*i.e.,* ref-, PEIE-, and mixed-SnO_2). The PEIS and photocurrent transient measurements were performed under 1 sun illumination in a 1 M KOH electrolyte (pH 14) at 0.5 and 1.0 V_{RHE}, respectively.

Author Manuscript

This article is protected by copyright. All rights reserved.

Author Manuscript

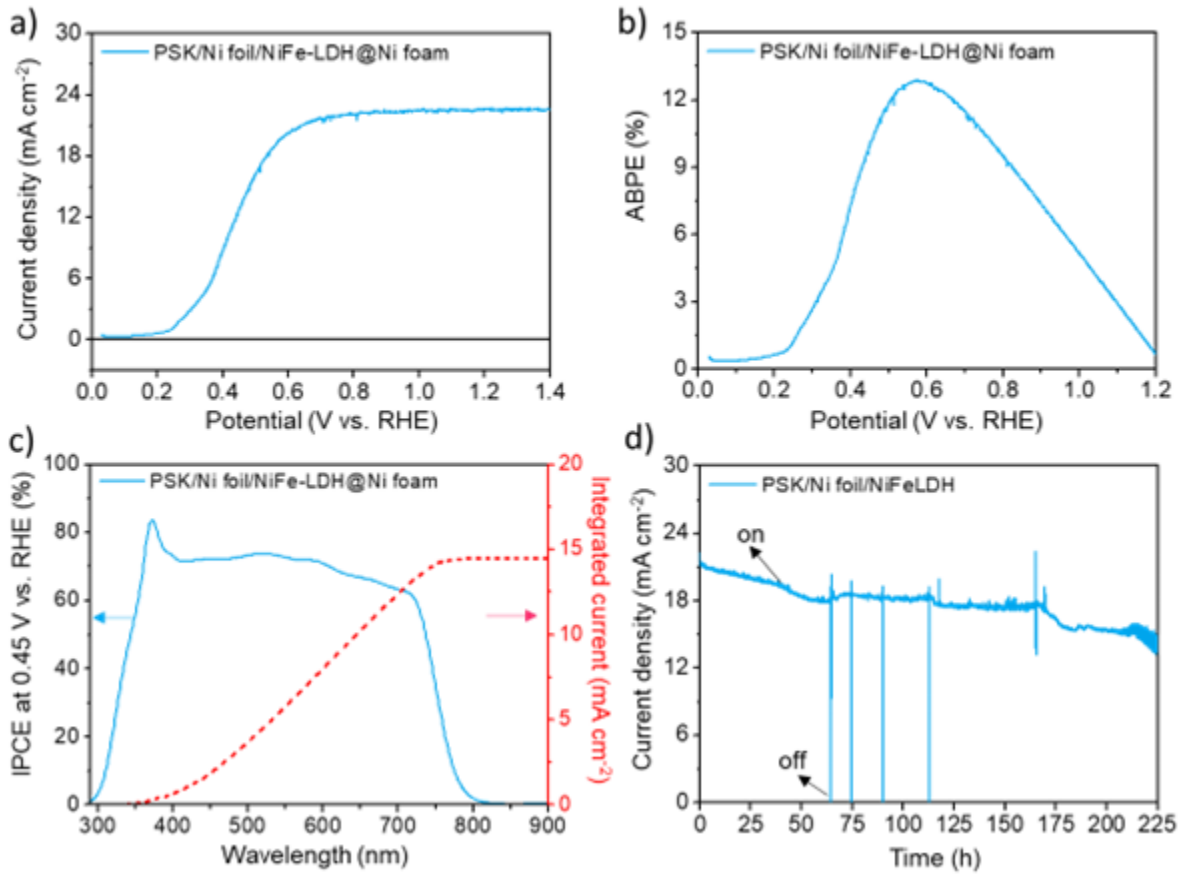


Figure 4. a) LSV curve of the PSK/Ni foil/NiFe-LDH@Ni foam photoanode in a 1 M KOH electrolyte (pH 14) under 1 sun illumination. b) ABPE and c) IPCE of the PSK/Ni foil/NiFe-LDH@Ni foam photoanode. d) The photocurrent stability test of the PSK/Ni foil/NiFe-LDH@Ni foam photoanode was performed at 1.23 V_{RHE} under 1 sun illumination.

This article is protected by copyright. All rights reserved.

Author Manuscript

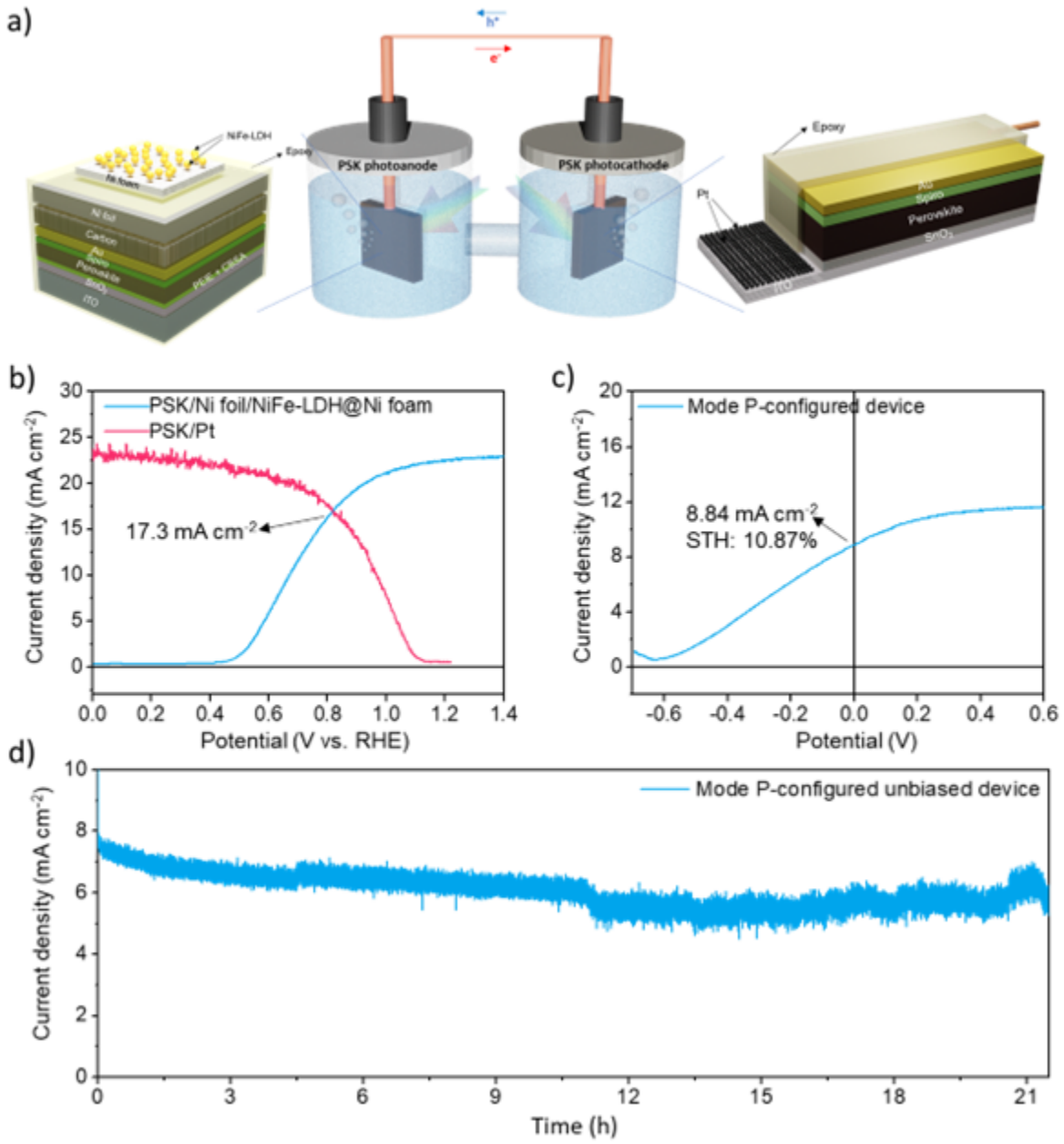


Figure 5. a) Schematic illustration of the PSK Mode P configuration. b) LSV curves of the PSK/Ni foil/NiFe-LDH@Ni foam photoanode and PSK/Pt photocathode in 0.5 M KPi (pH 7) under 1 sun illumination. The operating point of the Mode P-configured photoelectrode

This article is protected by copyright. All rights reserved.

is indicated as well. c) LSV curve and d) operational stability of the PSK Mode P-configured photoelectrode without any applied bias in 0.5 M KPi (pH 7) under 1-sun dual illumination on both the PSK photoanode and photocathode.

Author Manuscript

This article is protected by copyright. All rights reserved.

Author Manuscript

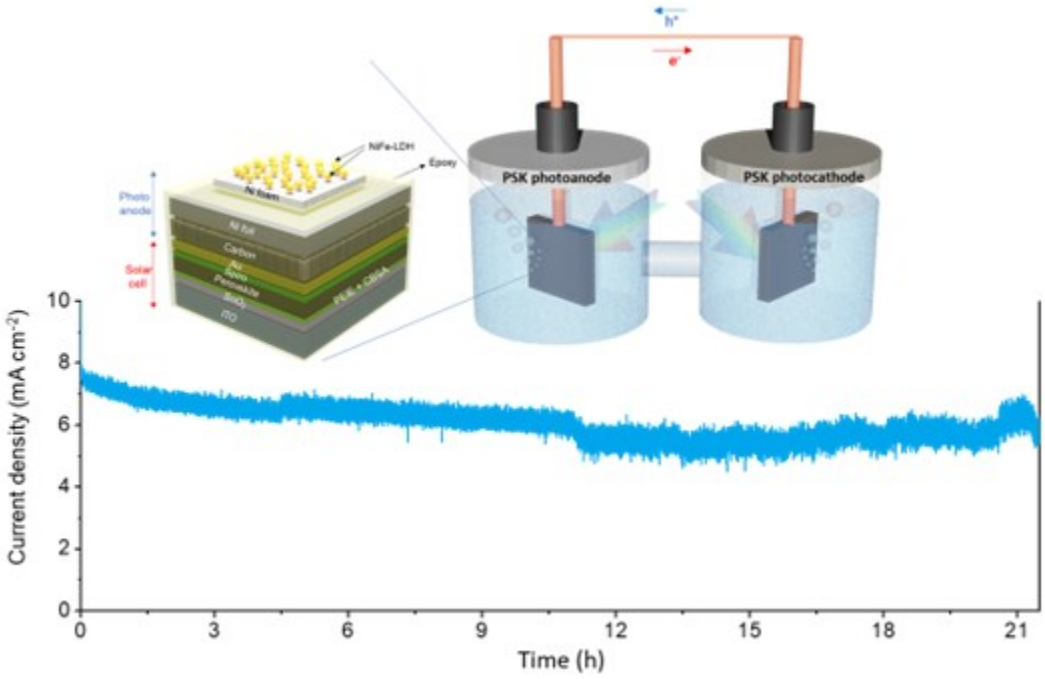
The combined application of polyethylenimine ethoxylated (dipole interlayer) and **chlorobenzenesulfonic acid** (passivator) at the SnO_2/perovskite interface of a perovskite photoanode drastically enhances its performance and stability up to 225 h. By pairing the perovskite photoanode with a perovskite photocathode, a bias-free solar water splitting was successfully demonstrated with a record-high efficiency (~10.9%) and reasonable stability of 22 h.

Keywords: perovskite photoanode, interface engineering, conductive passivation, interface dipole, unbiased water splitting

J. Yun, Dr. H. Lee, Y. S. Park, W. Jeong, C-S. Jeong, J. Lee, J. Lee, Dr. J. Tan, Dr. S. Ma, G. Jang, C. U. Lee, S. Moon, H. Im, S. Lee, D-Y. Yee, Prof. J-H. Kim, and Prof. J. Moon

This article is protected by copyright. All rights reserved.

Author Manuscript



This article is protected by copyright. All rights reserved.